BIOCELL

Tech Science Press

http://doi.org/10.32604/biocell.2026.081235

ARTICLE

Salviadione Attenuates Acute Lung Injury by Targeting VDAC1-Mediated Mitochondrial Ferroptosis

Wentao Su[1,#], Aishan Gulijiakela[1,#], Jihao Xiong[1], San Zhang[1] and Ke Ma[2,*]

[1]Department of Emergency, Huashan Hospital, Fudan University, Shanghai, China
[2]Department of Intensive Care Unit, Huashan Hospital, Fudan University, Shanghai, China
*Corresponding Author: Ke Ma. Email: hsh7makege@sohu.com
#These authors contributed equally to this work

Received: 26 February 2026; Accepted: 15 May 2026; Published: 26 August 2026

ABSTRACT: Objective: Mitochondrial dysfunction and ferroptosis contribute critically to acute lung injury (ALI), yet therapies targeting this pathway remain limited. This study investigates whether Salviadione, a rare alkaloid, protects against lipopolysaccharide (LPS)-induced epithelial damage by modulating the mitochondrial ferroptosis pathway. **Methods:** Network pharmacology, molecular docking, and molecular dynamics simulations identified potential targets. An *in vitro* model of lung epithelial injury was established using BEAS-2B cells exposed to LPS. Cell viability, lactate dehydrogenase (LDH) release, lipid peroxidation, Fe^{2+} accumulation, glutathione peroxidase 4 (GPX4) and acyl-CoA synthetase long-chain family member 4 (ACSL4) expression, mitochondrial membrane potential ($\Delta\Psi m$), mitochondrial reactive oxygen species (ROS), and ATP content were measured. voltage-dependent anion channel 1 (VDAC1) silencing and ferroptosis modulators (RSL3, ferrostatin-1) were used for mechanistic validation. **Results:** Salviadione (10 μM) increased LPS-reduced cell viability from 48.2 ± 3.1% to 82.5 ± 2.7% ($p < 0.05$) and decreased LDH release by 41.3% ($p < 0.05$). It reduced lipid peroxidation (by 58.6%, $p < 0.05$) and Fe^{2+} accumulation (by 47.2%, $p < 0.05$), restored GPX4 expression (to 86.4 ± 4.2% of control), and normalized ACSL4. Mitochondrial $\Delta\Psi m$ improved by 2.1-fold ($p < 0.01$), mitochondrial ROS decreased by 53.4% ($p < 0.05$), and ATP content increased by 2.3-fold ($p < 0.05$) versus LPS alone. VDAC1 knockdown abolished Salviadione's protective effects, while RSL3 reversed and ferrostatin-1 enhanced its actions. **Conclusion:** Salviadione protects lung epithelial cells from LPS-induced injury by stabilizing VDAC1, preserving mitochondrial function, and inhibiting ferroptosis via the VDAC1/GPX4 axis. These findings establish a foundation for Salviadione-based therapies targeting mitochondrial ferroptosis in ALI.

KEYWORDS: Salviadione; acute lung injury; ferroptosis; BEAS-2B cells; mitochondrial dysfunction; voltage-dependent anion channel 1 (VDAC1); glutathione peroxidase 4 (GPX4)

1 Introduction

Acute lung injury (ALI) may progress to the more severe acute respiratory distress syndrome (ARDS), both of which have major potential life-threatening consequences for clinical patients [1]. Excessive and dysregulated inflammation in the lung develops in response to multiple types of pulmonary insults, both direct and indirect. Excessive inflammation damages the alveolar–capillary barrier, causing increased vascular leakage, pulmonary edema, and persistent hypoxemia [2–4]. The underlying etiologies for ALI/ARDS are exceptionally heterogeneous and include severe infections, most notably sepsis, trauma, aspiration, and acute pancreatitis. Data demonstrate that these conditions continue to have high incidence and mortality in the Intensive Care Unit (ICU) [5]. While there have been significant advances in supportive

management, including lung-protective mechanical ventilation and optimized fluid strategies, overall mortality rates are still between 30% and 40%. This unsatisfactory outcome is largely attributed to the lack of effective pharmacological tools that can specifically target critical pathophysiological processes that underlie the development of the disease [6]. Therefore, the elaborate pathways that underlie the pathogenesis of ALI/ARDS and the identification of efficacious and safe therapeutic tools remain major challenges to the practice of respiratory and critical care medicine [7,8].

Damage and loss of alveolar epithelial cells disrupt the alveolar barrier and exacerbate lung edema in ALI [9]. Classical cell death mechanisms (apoptosis, necrosis) contribute to this process [10,11]. But recent attention has focused on ferroptosis—an iron-dependent, lipid peroxidation-driven cell death distinct from apoptosis and necrosis [12–14]. Ferroptosis is characterized by GPX4 inactivation, lipid ROS accumulation, and Fe^{2+}-driven Fenton chemistry [15–17]. Alveolar epithelial cells undergo ferroptosis in ALI models, and pharmacological inhibition of ferroptosis (e.g., ferrostatin-1) attenuates lung injury [18–21]. Mitochondria play a central role in ferroptosis, exhibiting loss of cristae, membrane potential collapse, and increased ROS production, which in turn amplify ferroptotic signaling [22,23].

Voltage-Dependent Anion Channel 1 (VDAC1), the major outer mitochondrial membrane pore protein, regulates the movement of metabolites, Ca^{2+} ions, and nucleotides between the mitochondria and the cytosol and hence maintains the mitochondrial function and the overall cell equilibrium [24]. Current evidence points to VDAC1 defects, which include abnormal opening or oligomerization, as a causative factor in cell death for a wide range of pathological conditions [25]. In the process of ferroptosis, VDAC1 is now seen as a central regulatory node in connecting external signals to mitochondrial damage [26]. Notably, some of the ferroptosis-inducing compounds, such as erastin, either directly or indirectly modulate VDAC1 and induce the activation of VDAC1, thereby mediating mitochondrial membrane depolarization, respiratory chain dysfunction, and increased ROS levels, ultimately impacting iron, promoting lipid peroxidation, and actively initiating the ferroptotic process [27]. Thus, targeting VDAC1 for the maintenance of mitochondrial integrity may be a promising step to modulate upstream targets in ferroptosis, leading to wide-ranging cytoprotective activities. However, the role of VDAC1 in the context of ferroptosis in ALI, as well as the modulating capacity of VDAC1 to prevent or attenuate ALI, has not been sufficiently explored.

GPX4 has been identified as an essential anti-ferroptotic enzyme that utilizes the reducing activity of glutathione to degrade phospholipid hydroperoxides into their corresponding alcohols, effectively halting the lipid peroxidation cascade [28]. Consequently, the attenuation of GPX4 at the protein level or the inactivation of its enzymatic activity represents a critical step in the execution of ferroptotic cell death. Interestingly, recent data indicate a complex relationship between VDAC1 and GPX4; for instance, inhibition of VDAC1 has been shown to preserve GPX4 expression in models of ischemia-reperfusion injury [29,30], and disruption of the GPX4-VDAC1 interaction promotes ferroptosis [31]. Maintenance of mitochondrial integrity is necessary for the perpetuation of GPX4 function and glutathione levels via continuous regeneration [32]. Oxidative stress and mitochondrial failure due to VDAC1 dysfunction may impair the antioxidant status of the cells, thereby hastening GPX4 depletion. Conversely, maintenance of mitochondrial function via suppression of abnormal activation of VDAC1 helps sustain the GPX4 antioxidant system [33,34]. Thus, this "VDAC1-mitochondrial function-GPX4 axis" defines a discrete pathway in which previously described elements co-exist in a rational manner. This signaling pathway is most likely a significant contributor to the pathogenesis of ALI. Its regulatory mechanisms and potential as a target need to be validated.

The identification of lead compounds of natural origin with simultaneous ability to interact with various targets and modulate critical pathological mechanisms is considered a promising approach to drug discovery [35–37]. Salviadione is a rare diterpenoid quinone alkaloid found in a historically employed

medicinal plant. Preliminary data on the pharmacological activities of this type of compound suggest their potential anti-inflammatory and antioxidant effects [38]. So far, it has not been investigated by researchers whether Salviadione exerts protective effects in respiratory diseases, including ALI. More importantly, whether its biological actions are linked with the increasingly recognized mitochondrial–ferroptosis axis remains wholly unexplored. Considering the knowledge gap, the mechanism whereby Salviadione preserves lung epithelial cells from lipopolysaccharide (LPS)-induced damage, and whether this is achieved through the modulation of the VDAC1/GPX4 mitochondrial ferroptosis cascade, was explored in this study. Network pharmacology methods were initially used to construct a global "compound-target-disease" network, which allowed the prediction and prioritization of the target and signaling pathways for the action of Salviadione in ALI. We also specifically examined the networks concerning ferroptosis and mitochondrial signaling. Finally, molecular docking and molecular dynamics simulations were carried out to examine the patterns of association as well as the binding stability of Salviadione with its major predicted targets, namely VDAC1 and GPX4, at atomic resolution. Following the *in silico* study, we induced LPS-mediated damage in human lung epithelial cells and studied the impact of Salviadione on various aspects, including cell survival, membrane integrity, ferroptosis biomarkers, and aspects of mitochondriopathy, such as changes in membrane potential, ROS, and aspects of metabolism. Finally, genetic loss-of-function strategies, including siRNA knockdown of VDAC1, together with pharmacological modulation using the ferroptosis inducer RSL3 and inhibitor ferrostatin-1, were employed to examine the causal roles of the identified targets and signaling pathways involved. Using these approaches, we investigated whether VDAC1 was necessary for Salviadione-mediated protection and whether its major mechanism involved the suppression of a form of programmed cell death called ferroptosis.

Human bronchial epithelial BEAS-2B cells were selected for this study because they are a well-characterized, non-tumorigenic cell line that retains key features of normal airway epithelial cells and has been widely used in LPS-induced acute lung injury models [39–41]. This *in vitro* model allows controlled, reproducible investigation of molecular mechanisms at the cellular level prior to *in vivo* validation. Using network pharmacology, we initially predicted that VDAC1 and GPX4 are among the top targets of Salviadione in acute lung injury, leading us to focus on this axis for subsequent experimental validation. Thus, our investigation is expected to establish the protective function of Salviadione in lung epithelial cells and define its unique molecular mechanism, considering the promising natural scaffold for ALI therapy and implying the revelation of a novel regulatory node involved in the pathogenesis of diseases. This study focuses on the "VDAC1–mitochondrial function–GPX4–ferroptosis" axis in search of an unappreciated connection between organelle stress and ferroptotic cell death in ALI, hence providing new experimental insights and conceptual frameworks for understanding disease pathology. Although LPS was used to model inflammation-induced injury, the primary focus of this study is on cellular injury and ferroptosis, not on the measurement of inflammatory mediators per se.

2 Material and Methods

2.1 Network Pharmacology Analysis

2.1.1 Disease and Drug Target Collection and Preprocessing

The ALI-associated disease targets were obtained by integrating information from multiple sources. Through using the keyword "Acute Lung Injury", we retrieved relevant genes from the Genecards (https://www.genecards.org/), OMIM (https://www.omim.org/), and PharmGKB (https://www.clinpgx.org/) databases. Meanwhile, the ALI-related gene expression dataset GSE226486 was downloaded from the GEO database (https://www.ncbi.nlm.nih.gov/geo/), and then differential expression analysis was performed

using the "limma" package (version 3.54.0) in R (version 4.2.0). Batch effects were corrected using the ComBat function in the "sva" package, with the study batch included as a covariate. By the criterion of $|\log_2\text{FoldChange}| > 1$ and adjusted p-value < 0.05, we identified significantly differentially expressed genes. These thresholds are widely accepted in transcriptomic analyses: $|\log_2\text{FC}| > 1$ corresponds to a two-fold change, ensuring biological relevance, while an adjusted p-value < 0.05 controls the false discovery rate below 5%. Then we merged the gene sets from both sources, removed duplicates, and standardized them with the UniProt database (https://www.uniprot.org/) for uniform gene nomenclature. The resulting curated collection constituted the comprehensive ALI disease target set (Set_ALI).

The SMILES structure of Salviadione (CC(C)C1=CC2=C3C4=C(C=C2)C(CC(=C4N=C3C1=O)O)(C)C) was obtained from the PubChem database (CID: 135442608, https://pubchem.ncbi.nlm.nih.gov/) and uploaded to the SwissTargetPrediction (https://www.swisstargetprediction.ch/) and PharmMapper (http://www.lilab-ecust.cn/pharmmapper/) platforms to predict potential targets, with a filtering threshold of Probability > 0. All predicted gene names were standardized via the UniProt database. To specifically focus on ferroptosis- and mitochondria-related mechanisms, ferroptosis-associated genes were retrieved from FerrDb V3 (https://www.zhounan.org/ferrdb/v3/pages/index.html; Set_Ferroptosis), and mitochondria-related genes were obtained from MitoCarta3.0 (https://www.broadinstitute.org/mitocarta/mitocarta30-inventory-mammalian-mitochondrial-proteins-and-pathways; Set_Mitochondria). All gene symbols were standardized using UniProt to ensure consistency.

2.1.2 Core Target Screening

Using the collected gene sets, we conducted a multi-level Venn diagram analysis to screen for core targets. First, the predicted targets of Salviadione (Set_Drug) were intersected with ALI-associated genes (Set_ALI) to obtain the shared drug–disease targets. This set was then further intersected with ferroptosis-related genes (Set_Ferroptosis) and mitochondria-related genes (Set_Mitochondria). The genes present in the final intersection were designated as the "core mitochondrial ferroptosis-related ALI targets" (Core_Targets) for subsequent analyses. All Venn diagrams were generated using the "VennDiagram" (version 1.7.3) package in R, with the number of genes in each region clearly annotated.

To prioritize the most relevant targets for subsequent validation, we applied the following criteria: (i) genes present in the intersection of Salviadione-ALI targets, ferroptosis genes, and mitochondria-related genes (Core_Targets); (ii) high degree centrality in the PPI network (top 10% by degree); and (iii) strong binding affinity to Salviadione as assessed by molecular docking. Among the Core_Targets, VDAC1 and GPX4 consistently met all three criteria: both were identified as hub genes (top 10 in CytoHubba MCC ranking), and molecular docking revealed favorable binding energies (VDAC1: −8.4 kcal/mol, GPX4: −7.0 kcal/mol; see Section 3.2). Therefore, VDAC1 and GPX4 were selected as the primary targets for further mechanistic investigation. Thus, the core targets were identified through a stepwise filtration strategy: (i) intersection of drug targets with ALI-associated genes; (ii) further intersection with ferroptosis- and mitochondria-related gene sets; (iii) topological analysis of the PPI network to prioritize hub genes; and (iv) molecular docking to validate binding affinity. This multi-level filtration reduces false positives and focuses on mechanistically relevant targets.

2.1.3 Protein–Protein Interaction (PPI) Network Construction and Topological Analysis

We submitted the Core_Targets to the STRING database (version 11.0), limiting the species to Homo sapiens and setting a high-confidence threshold of 0.700, while hiding disconnected nodes, to generate a protein–protein interaction (PPI) network. We imported the interaction data into Cytoscape (version 3.10.2)

to enable visualization and downstream analysis. Topological parameters of the network, such as degree, betweenness centrality, and closeness centrality, were computed using the NetworkAnalyzer tool. We used the MCODE plugin to find tightly connected functional modules. The parameters for the module search were set as follows: Degree Cutoff = 2, Node Score Cutoff = 0.2, K-Core = 2, and Max. Depth = 100. We marked the module with the highest MCODE score as Cluster 1 (MCODE Score = 9). In addition, we used the MCC (Maximal Clique Centrality) algorithm in the CytoHubba plugin to screen hub genes in the network and marked the top 10 genes as key hubs. Notably, the highest-scoring Cluster 1 showed a high degree of overlap with these top 10 hub genes.

2.1.4 Functional and Pathway Enrichment Analysis

To explore the functional implications of the core targets in biological processes, cellular components, molecular functions, and signaling pathways, we used systematic enrichment analyses. Accordingly, GO and KEGG pathway enrichment analyses were conducted on two different gene sets: (1) all Core_Targets, and (2) the top 10 hub genes as determined using the MCC algorithm. We carried out the enrichment analyses using the R package "clusterProfiler" (version 4.10.0), applying an adjusted p-value < 0.05 (Benjamini–Hochberg correction) as the criterion for significance. We visualized the outcomes by using bubble and bar plots showing enriched terms, associated gene counts, enrichment factors, and statistical significance.

2.2 Molecular Docking

We carried out molecular docking using AutoDock Vina v1.2.5 (https://vina.scripps.edu/). Crystal structures of human VDAC1 and GPX4 were retrieved from the Protein Data Bank (https://www.rcsb.org/). Protein files were converted using Open Babel v3.1.1 (http://openbabel.org/) and subsequently prepared in AutoDock Tools v1.5.7 (http://mgltools.scripps.edu/) for the elimination of water molecules, addition of hydrogen atoms, energy minimization, and calculation of Gasteiger charges. The Salviadione small-molecule structure was prepared using Open Babel v3.1.1 and RDKit v2023.09.1 (https://www.rdkit.org/) for format conversion, energy minimization, and 3D optimization, followed by hydrogen addition, charge calculation, and final PDBQT conversion in AutoDock Tools. Docking grid boxes were defined as follows: for VDAC1, the box center was set at (5.163, 1.548, 0.034) Å with grid dimensions of 54 × 44 × 40 points and a spacing of 1.0 Å in each direction; for GPX4, the box center was (6.246, −19.721, −17.774) Å with grid dimensions of 42 × 48 × 66 points and the same spacing. All docking runs searched within an energy range of ±5 kcal/mol and generated 20 binding modes (num_modes = 20) to ensure adequate sampling. Default docking parameters were applied, with adjustments only to grid box position and size to match the active pockets of the proteins. Docking results were output as log files, and the binding affinities (kcal/mol) were inspected using a text editor. We chose the conformation with the lowest binding energy as the optimal binding mode for further analyses. The calculated binding energies for Salviadione with VDAC1 and GPX4 were −8.4 kcal/mol and −7.0 kcal/mol, respectively, indicating strong and stable interactions.

2.3 Molecular Dynamics Simulation

The most stable Salviadione–VDAC1 complex obtained from molecular docking was selected for 100 ns molecular dynamics (MD) simulation. Simulations were performed using GROMACS 2024. Protein topology was generated with the gmx pdb2gmx module using the AMBER14 force field and TIP3P water model. The ligand topology was prepared with the sobtop tool based on the GAFF force field, and RESP2 charges were derived from ORCA wavefunction calculations, with geometry optimization at the B97-3c level. We placed the system in a cubic periodic box with a 1.0 nm buffer, solvated it with the SPC216 water model,

and added Na^+ and Cl^- ions for neutralization. Following energy minimization, we equilibrated the system under NVT and NPT ensembles. Temperature was maintained at 300 K using the V-rescale thermostat, and pressure was adjusted with the Berendsen barostat. Production simulations were run using the leap-frog integrator, saving trajectories every 10 ps. We constrained bond lengths with the LINCS algorithm and handled long-range electrostatics with the PME method, applying a 1.0 nm cutoff. Complex stability was analyzed via root-mean-square deviation (RMSD) and root-mean-square fluctuation (RMSF), and binding free energies were estimated through MM/PBSA or MM/GBSA calculations. The solvent-accessible surface area (SASA) was calculated using the gmx sasa tool of GROMACS with a probe radius of 1.4 Å. The Gibbs free energy landscape was constructed based on the first two principal components (PC1 and PC2) derived from covariance analysis of the Cα atoms, using the gmx sham tool. Electrostatic surface potential maps were generated using the APBS plugin in PyMOL (v2.5) with the Poisson–Boltzmann method, and visualized with the PyMOL molecular graphics system.

2.4 Cell Experiments

2.4.1 Cell Culture

BEAS-2B human lung epithelial cells were sourced from the Cell Bank/Stem Cell Bank, Chinese Academy of Sciences (Shanghai, China; https://www.cellbank.org.cn). According to the supplier, each batch of BEAS-2B cells has been authenticated by short tandem repeat (STR) profiling and tested negative for mycoplasma contamination. Cells were cultured in RPMI-1640 medium (Gibco, Thermo Fisher Scientific, Waltham, MA, USA; Cat# 11875093) enriched with 10% fetal bovine serum (FBS; Gibco, Cat# 10099141) and 1% penicillin–streptomycin (Gibco, Cat# 15140122) at 37°C under humidified conditions with 5% CO_2. The culture medium was renewed every two days.

2.4.2 LPS-Induced Cell Injury Model and Drug Treatment

Preliminary experiments were conducted to ascertain the most effective concentrations of LPS and Salviadione for inducing cell injury. We incubated BEAS-2B cells with LPS (lipopolysaccharide from Escherichia coli O111:B4, Cat# L4391, Sigma-Aldrich, St. Louis, MO, USA) at 0, 0.1, 0.5, 1, 5, and 10 μg/mL for 24 h and measured cell viability using the CCK-8 assay. A concentration that reduced cell viability by 40%–60% (1 μg/mL) was selected to induce cell injury. We screened Salviadione (purity ≥ 98%, Cat# SMB00987, Sigma-Aldrich, St. Louis, MO, USA) at 0, 2.5, 5, 10, 20, and 40 μM using this LPS-induced model and selected 5, 10, and 20 μM as low, medium, and high doses for follow-up experiments. These concentrations were chosen because they dose-dependently restored LPS-reduced cell viability (from 5 μM to 20 μM) in preliminary experiments without causing any cytotoxicity, as confirmed by LDH release assays in preliminary experiments. The highest tested concentration (40 μM) did not provide additional benefit and was therefore not used. For the main experiment, the cells were categorized into six groups: control, vehicle control (0.1% DMSO), LPS model (1 μg/mL), LPS with Salviadione at low, medium, and high doses (1 μg/mL + 5, 10, 20 μM), and Salviadione alone (10 μM).

2.4.3 Cell Viability and Cytotoxicity Assays

The cells are plated as monolayers in a 96-well culture plate at a density of 1×10^4 cells per well and treated as required. Cellular viability was measured using a CCK-8 assay kit (Beyotime, Shanghai, China; Cat# C0046) to detect absorbance at a wavelength of 450 nm using a microplate reader (BioTek Synergy H1, Agilent Technologies, Santa Clara, CA, USA). The activity of LDH released was investigated using a commercial kit (Beyotime, Cat# C0016), detecting absorbance at a wavelength of 490 nm on the same microplate reader.

2.4.4 Lipid ROS Measurement

Lipid reactive oxygen species can be detected by fluorescent probes such as the probe (Invitrogen, Thermo Fisher Scientific, Waltham, MA, USA; Cat# D3861). After treatment, BEAS-2B cells were incubated with 2 μM C11-BODIPY 581/591 in serum-free medium at 37°C for 30 min in the dark. Cells were then washed twice with PBS, trypsinized, and resuspended in PBS containing 1% FBS. Fluorescence intensity was analyzed using a flow cytometer (BD FACSCanto II, BD Biosciences, San Jose, CA, USA) with excitation at 488 nm and emission at 530 nm (oxidized form) and 585 nm (reduced form). Data were processed using FlowJo software (v10.8). The shift in fluorescence from red to green indicates lipid peroxidation, and results are presented as the ratio of mean fluorescence intensity (MFI) of oxidized to reduced probe.

2.4.5 Intracellular Fe^{2+} Measurement

Intracellular ferrous iron (Fe^{2+}) levels can be detected by the FerroOrange probe (Biotium, Hayward, CA, USA; Cat# 20235). Following treatment, cells were incubated with 1 μM FerroOrange in HBSS at 37°C for 30 min in the dark. After washing twice with HBSS, fluorescence images were captured using an inverted fluorescence microscope (Olympus IX73, Olympus Corporation, Tokyo, Japan) with excitation at 561 nm and emission at 570–620 nm. Fluorescence intensity was quantified using ImageJ software (version 1.53c, National Institutes of Health, Bethesda, MD, USA) from at least five random fields per well.

2.4.6 Western Blotting

Total protein was extracted using RIPA lysis buffer (Beyotime, Shanghai, China; Cat# P0013B) containing protease inhibitors. Protein concentrations were determined using a BCA kit (Beyotime, Cat# P0006). Equal amounts of protein (20 μg per lane) were separated by 12% SDS-PAGE and transferred to PVDF membranes (Millipore, Burlington, MA, USA; Cat# IPVH00010). Membranes were blocked with 5% non-fat milk in TBST for 1 h at room temperature and then incubated overnight at 4°C with primary antibodies: anti-GPX4 (Abcam, Cambridge, UK; Cat# ab124978, 1:1000 dilution), anti-ACSL4 (Proteintech, Rosemont, IL, USA; Cat# 12788-1-AP, 1:1000 dilution), anti-VDAC1 (Abcam, Cambridge, UK; Cat# ab158957, 1:1000), anti-COX IV (Proteintech, Rosemont, IL, USA; Cat# 10865-1-AP, 1:1000), and anti-β-actin (Santa Cruz Biotechnology, Dallas, TX, USA; Cat# sc-47778, 1:5000 dilution) as a loading control. After washing, membranes were incubated with HRP-conjugated secondary antibodies (anti-rabbit IgG, Abcam, Cat# ab205718, 1:5000; anti-mouse IgG, Abcam, Cat# ab205719, 1:5000) for 1 h at room temperature. Signals were visualized using ECL substrate (Thermo Fisher Scientific, Waltham, MA, USA; Cat# 34077). Band intensities were quantified using ImageJ software, normalized to β-actin. All western blot experiments were independently repeated three times (n = 3 biological replicates), and representative blots are shown. The same procedure was used to detect VDAC1, GPX4, and COX IV in mitochondrial-related experiments.

2.4.7 Pharmacological Ferroptosis Modulation

To affirm the involvement of ferroptosis in the LPS-induced damage, additional experimental groups were introduced: LPS + Ferrostatin-1 (Fer-1, 1 μM), Erastin (10 μM, positive control), and Erastin + Salviadione (10 μM). Ferrostatin-1 and Erastin were purchased from MedChemExpress (MCE, Monmouth Junction, NJ, USA; Cat# HY-14397 and HY-12023, respectively).

2.4.8 Mitochondrial Membrane Potential ($\Delta\Psi m$)

Mitochondrial membrane potential was assessed using the JC-1 dye (Beyotime, Shanghai, China; Cat# C2018). After treatment, BEAS-2B cells were incubated with JC-1 (5 μg/mL) in culture medium at 37°C for 30 min in the dark. Cells were then washed twice with PBS, trypsinized, and resuspended in PBS. Fluorescence was analyzed using a flow cytometer (BD FACSCanto II, BD Biosciences, San Jose, CA, USA) with excitation at 488 nm and emission at 530 nm (green, monomeric form) and 585 nm (red, J-aggregate form). The ratio of red to green fluorescence intensity was calculated to represent ΔΨm. Data were processed using FlowJo v10.8.

2.4.9 Mitochondrial Reactive Oxygen Species (mitoROS)

Mitochondrial ROS levels were detected using MitoSOX^{TM} Red reagent (Thermo Fisher Scientific, Waltham, MA, USA; Cat# M36008). Cells were incubated with 2.5 μM MitoSOX in HBSS at 37°C for 30 min in the dark, washed twice with PBS, trypsinized, and resuspended in PBS. Fluorescence was measured using the same flow cytometer (BD FACSCanto II) with excitation at 488 nm and emission at 580 nm. Data were analyzed with FlowJo v10.8, and results are presented as mean fluorescence intensity (MFI) relative to control.

2.4.10 ATP Content Measurement

Intracellular ATP levels were measured using a chemiluminescence-based ATP assay kit (Beyotime, Cat# S0026S) according to the manufacturer's instructions. Briefly, after treatment, cells were lysed with the provided lysis buffer, centrifuged at 12,000× *g* for 5 min at 4°C, and the supernatant was mixed with the luciferase reagent. Luminescence was recorded using a microplate reader (BioTek Synergy H1, Agilent Technologies, Santa Clara, CA, USA). ATP content was normalized to total protein concentration and expressed as a percentage of the control group.

2.4.11 siRNA Transfection Experiments

We transfected BEAS-2B cells with VDAC1-targeting siRNA (RiboBio, Guangzhou, China, Cat# RIBO01273) and used a non-targeting siRNA (si-NC) as a negative control. The siRNA sequences were designed and synthesized by RiboBio. The targeting sequence for human VDAC1 was 5′-GGAAGAGAA AGGUAAUAAATT-3′ (sense) and 5′-UUUAUUACCUUUCUCUUCCTT-3′ (antisense). The negative control siRNA (si-NC) was a non-targeting scrambled sequence with no homology to any human gene, provided by the same manufacturer. We transfected cells using Lipofectamine® 3000 (Thermo Fisher Scientific, Cat# L3000015) and confirmed knockdown efficiency by Western blot 48 h post-transfection. Following confirmation, we applied the designated treatments to cells based on their experimental groups (si-NC or si-VDAC1 with LPS or LPS + Salviadione) to perform CCK-8 and lipid ROS assays.

2.4.12 Pharmacological Intervention Experiments

The cells received treatment with either RSL3 (50 nM; MedChemExpress, Cat# HY-12001) to induce ferroptosis or Ferrostatin-1 (1 μM; MedChemExpress, Cat# HY-14397) to inhibit ferroptosis. The concentration was selected based on previous studies showing effective ferroptosis induction in BEAS-2B cells [42]. We added RSL3 or Fer-1 during LPS and Salviadione co-treatment to investigate ferroptosis regulation. Cell viability, lipid ROS accumulation, and GPX4 protein levels were measured to analyze how these interventions influenced the cells.

2.4.13 qPCR Analysis

Total RNA was extracted from BEAS-2B cells using TRIzol reagent (Invitrogen, Thermo Fisher Scientific, Waltham, MA, USA; Cat# 15596018). RNA concentration and purity were assessed by measuring the absorbance ratio A_{260}/A_{280} using a NanoDrop spectrophotometer (Thermo Fisher Scientific, Waltham, MA, USA). Only samples with an A_{260}/A_{280} ratio between 1.8 and 2.0 were used for further analysis. Reverse transcription was performed using a PrimeScript RT reagent kit (Takara Bio Inc., Kusatsu, Shiga, Japan, Cat# RR037A). Specifically, 1 μg of total RNA was reverse transcribed in a 20-μL reaction volume under the following conditions: 37°C for 15 min, 85°C for 5 s, and then held at 4°C. Quantitative PCR was carried out using TB Green Premix Ex Taq II (Takara Bio, Cat# RR420A) on an ABI StepOnePlus Real-Time PCR System (Applied Biosystems, Thermo Fisher Scientific, Waltham, MA, USA). The thermal cycling protocol was: initial denaturation at 95°C for 30 s, followed by 40 cycles of 95°C for 5 s and 60°C for 34 s (annealing/extension). A dissociation stage (95°C for 15 s, 60°C for 1 min, 95°C for 15 s) was added to verify amplicon specificity. The primer sequences used for each gene were as follows: VDAC1: forward 5′-GGAGAGGAAGTTGCCAGTTC-3′, reverse 5′-ACAGTGCTGGTAGCCAGAAG-3′ (or provide your actual sequences); GPX4: forward 5′-GCCAAGAACGAAGAGATCCG-3′, reverse 5′-ACGGTCCATGTGATCGTCAG-3′; β-actin: forward 5′-CATGTACGTTGCTATCCAGGC-3′, reverse 5′-CTCCTTAATGTCACGCACGAT-3′.

Each reaction was performed in triplicate (technical replicates). The relative expression levels of target mRNAs were calculated using the $2^{-\Delta\Delta Ct}$ method, with β-actin as the internal reference gene. All experiments were independently repeated at least three times (n = 3 biological replicates), and the results are expressed as fold change relative to the control group.

2.4.14 General Experimental Design and Data Normalization

All experiments were independently repeated at least three times (n = 3 biological replicates), unless otherwise specified in the respective subsections. For each biological replicate, technical replicates (e.g., duplicate or triplicate wells) were included, and the mean value of technical replicates was treated as a single data point for subsequent statistical analysis. For quantitative assays (e.g., CCK-8, LDH, lipid ROS, Fe^{2+}, JC-1, MitoSOX, ATP, and Western blotting), data were normalized to the control group (set as 100% or 1-fold) or to the loading control (β-actin for Western blot), as indicated in the figure legends. All data are presented as mean ± SEM, and statistical comparisons were performed on the normalized values.

2.5 Statistical Analysis

We analyzed statistical data using GraphPad Prism v.10.1 (GraphPad Software, La Jolla, CA, USA). The Shapiro–Wilk test was used to verify the normal distribution of the datasets. For multiple group comparisons, we applied one-way ANOVA followed by Tukey's post hoc test, and for two-group comparisons, we performed unpaired Student's *t*-tests. Data are reported as mean ± standard error of the mean (SEM) (n = 3), with $p < 0.05$ indicating statistical significance.

3 Results

3.1 Network Pharmacology Predicts That Salviadione Exerts Pulmonary Protection via the VDAC1-GPX4 Axis by Modulating Mitochondrial Ferroptosis

To systematically investigate the potential mechanisms of Salviadione in acute lung injury (ALI), we integrated multiple databases and applied a network pharmacology approach for target identification and

pathway enrichment analysis. First, Venn diagram analysis of ALI-related gene sets from four independent sources (GSE226486, GeneCards, OMIM, and PharmGKB) identified a total of 13,517 ALI-associated genes. By integrating drug–target databases, 362 potential Salviadione targets were obtained. Notably, intersection analysis with ferroptosis-related genes (3483) and mitochondria-related genes (1136) revealed overlapping genes, providing preliminary clues for exploring the mechanisms of Salviadione (Fig. 1A). Further intersection of Salviadione predicted targets with ALI-associated genes yielded 198 common targets (361 drug-related and 13,517 disease-related targets; Fig. 1B), which were used to construct a compound–target–disease network (Fig. 1C). We identified VDAC1, GPX4, FASN, SIRT5, and CASP3 as key nodes, which likely contribute to the anti-inflammatory effects mediated by Salviadione. Based on the close relationship between ferroptosis and mitochondrial dysfunction, we investigated the genes that interact between the Salviadione targets and the genes related to mitochondrial dysfunction and ferroptosis signaling. We identified 28 genes that were linked to both ferroptosis and mitochondrial dysfunction, and 73 targets of Salviadione were linked to ferroptosis (Fig. 1D). This suggests that Salviadione exerts its cell protection by regulating the ferroptosis-related pathways.

We also used these targets, namely ALI-, Salviadione-, ferroptosis-, and mitochondria-related, to initiate the formation of a PPI network using Cytoscape. Network analysis of VDAC1 and GPX4 further showed their location in the center of highly connected core modules, with close connections to other proteins related to oxidative stress and metabolism (Fig. 1E,F). We used the MCC algorithm in CytoHubba to identify the top 10 hub genes and constructed a core subnetwork (Fig. 1G), which included ferroptosis key protein (GPX4, FASN) and mitochondria-related protein (VDAC1, NDUFS3). It is indicated that Salviadione mediates a protective role by modulating the "mitochondria-ferroptosis" network. GO and KEGG pathways confirmed that these major targets for NO donation in cells are engaged in biological processes such as fatty acid metabolism, responses to reactive oxygen species, mitochondrial membrane transport, and glutathione metabolism (Fig. 1H), suggesting that these proteins are engaged in redox balance and lipid metabolic regulation. Further enrichment analysis of the top 10 hub genes showed significant association with fatty acid metabolism, acyl-CoA metabolic processes, respiratory chain complex I, and NADH dehydrogenase complex (Fig. 1I), highlighting their central roles in energy metabolism and redox balance. Overall, our findings indicate that Salviadione preserves lung epithelial cell integrity in inflammation, at least partially through modulation of the VDAC1–GPX4-dependent mitochondrial ferroptosis pathway. We acknowledge that network pharmacology predictions are inherently computational and may include false positives due to database biases, incomplete interactomes, or indirect pharmacological effects. The identified targets (e.g., VDAC1 and GPX4) were therefore not accepted solely based on *in silico* scores; they were subsequently validated by molecular docking, molecular dynamics simulations, and cellular experiments. This integrated approach mitigates the limitations of pure prediction and strengthens confidence in target selection.

3.2 Molecular Docking Analysis of Salviadione with VDAC1 and GPX4

We performed molecular docking of Salviadione with VDAC1 and GPX4 using AutoDock Vina and found that Salviadione interacts with VDAC1 and GPX4. Our findings indicated that Salviadione established stable interactions with active pockets of VDAC1 (PDB: 5JDP) and GPX4 (PDB: 9RF1) (Fig. 2). Three-dimensional binding conformations of Salviadione with VDAC1 and GPX4 indicated stable interactions with functional groups of VDAC1 and GPX4 proteins (Fig. 2A,B). We created two-dimensional interaction diagrams to visualize the molecular interactions, using green dashed lines to represent hydrogen bonds and red concentric arcs to highlight hydrophobic contacts (Fig. 2C,D). These results support that Salviadione binds well to both VDAC1

and GPX4 and, thus, provide structural evidence for the hypothesis that Salviadione may exert its biological effects by modulation of the VDAC1-GPX4 pathway.

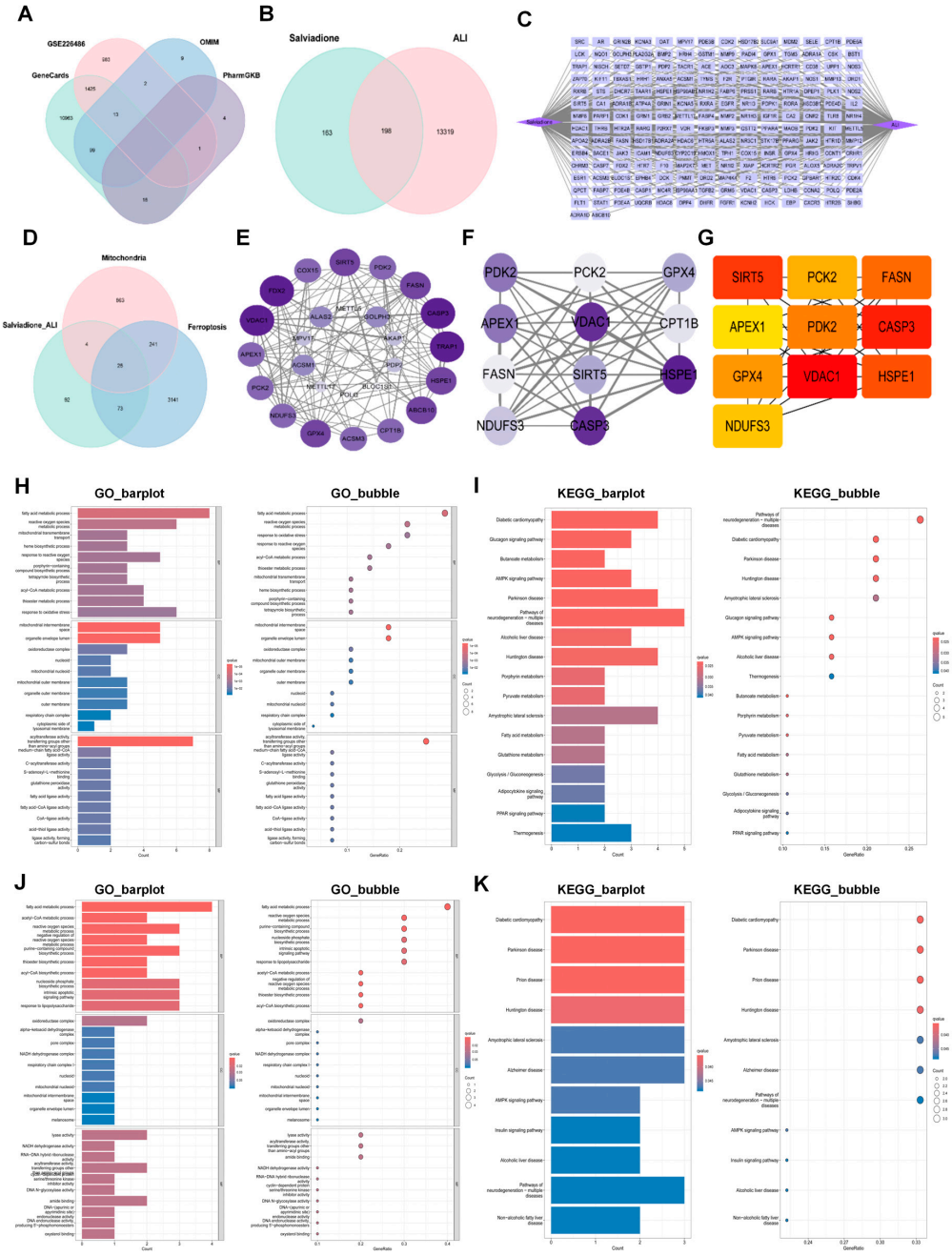

Figure 1: Network pharmacological screening of core targets for Salviadione in treating ALI. (**A**) Venn diagram of ALI-related targets collected from Genecards, OMIM, PharmGKB databases, and GSE226486 dataset. (**B**) Venn diagram showing the intersection between Salviadione-predicted targets and the integrated ALI targets. (**C**) Drug-Target-Disease network constructed with Salviadione, its overlapping targets with ALI, and the disease node. (**D**) Venn diagram identifying the core targets at the intersection of Salviadione-ALI targets, ferroptosis genes, and mitochondrial genes. (**E**) Protein-protein interaction (PPI) network of the core targets constructed using the STRING database. (**F**) The top functional modules (Cluster 1) were identified from the PPI network using the MCODE algorithm. (**G**) Sub-network of the top 10 hub genes identified from the PPI network using the MCC algorithm in

CytoHubba. (**H**) GO enrichment analysis of all core targets (Core_Targets). (**I**) KEGG pathway enrichment analysis of the Core_Targets. (**J**) GO enrichment analysis of the top 10 hub genes. (**K**) KEGG pathway enrichment analysis of the top 10 hub genes. For all Venn diagrams, numbers indicate the count of unique or overlapping genes. Networks were visualized using Cytoscape. Enrichment analysis was performed with a significance threshold of adjusted p-value < 0.05.

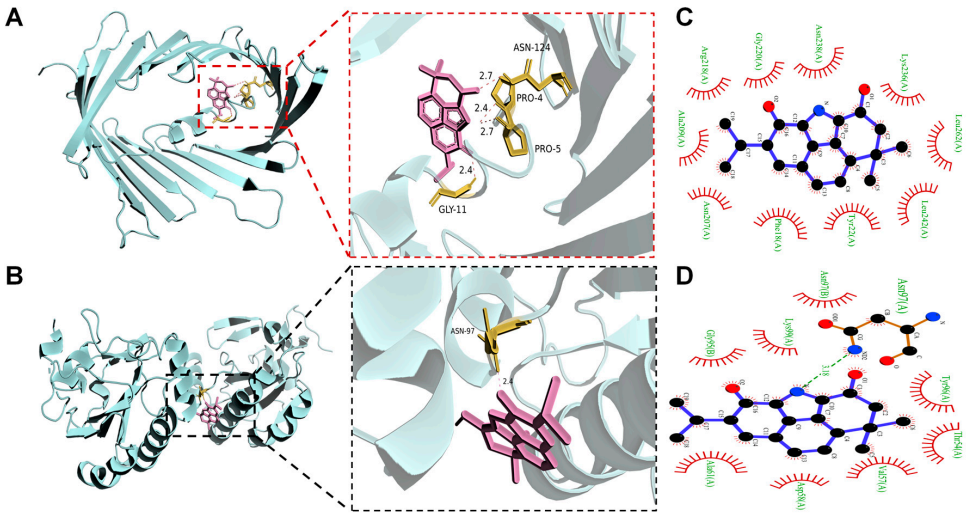

Figure 2: Molecular docking analysis of Salviadione binding to VDAC1 and GPX4. (**A**) Three-dimensional interaction mode of Salviadione within the binding pocket of VDAC1 (PDB: 5JDP). Key interacting residues are shown as sticks. (**B**) Three-dimensional interaction mode of Salviadione within the binding pocket of GPX4 (PDB: 9RF1). (**C**) Two-dimensional interaction diagram corresponding to (**A**), detailing hydrogen bonds and hydrophobic interactions. (**D**) Two-dimensional interaction diagram corresponding to (**C**). Molecular docking was performed using AutoDock Vina. Hydrogen bonds are shown as green dashed lines, and hydrophobic interactions are shown as red concentric arcs.

3.3 Molecular Dynamics Simulation Analysis of the Salviadione–VDAC1 Complex

To investigate the structural stability and binding characteristics of the Salviadione-VDAC1 complex, a molecular dynamics simulation of 100 ns was carried out. From the root mean square deviation (RMSD) plot of the complex (Fig. 3A), the system was able to achieve equilibrium at 40 ns, whereby the backbone RMSD, the overall protein-ligand complex RMSD, and the ligand RMSD were maintained at 0.65 ± 0.03 Å, 0.68 ± 0.03 Å, and 0.05 ± 0.01 Å, respectively. Next, root-mean-square fluctuation (RMSF) analysis (Fig. 3B) revealed that the high flexibility regions were centered around 100–150 and 250–300, which probably included the loop and β-turn regions, while the binding pocket was highly stable in terms of RMSF. From the result obtained in the analysis, the solvent-accessible surface area was observed to be stable at about 184.5 ± 2.7 $Å^2$ (Fig. 3C). The radius of gyration was stable throughout the simulation (Fig. 3D), implying the folded conformation of the complex. The hydrogen bonds formed between Salviadione and VDAC1 were consistently maintained at 1–2 hydrogen bonds, with some slight fluctuations up to 3 hydrogen bonds (Fig. 3E).

MM/GBSA binding free energy calculation (Fig. 3F) showed that the total binding free energy was −23.01 kcal/mol. Van der Waals interaction (−35.85 kcal/mol) was strong while electrostatic interaction (−13.68 kcal/mol) drove the binding process. However, polar solvation energy was unfavorable in that it added up to 29.86 kcal/mol, while the nonpolar solvation energy added up to −3.35 kcal/mol. The per-residue energy decomposition analysis (Fig. 3G) showed that residues such as CYS127, LYS115, and GLY126 contributed significantly to the binding free energy, indicating their role as interaction sites. The Gibbs free energy landscape (Fig. 3H,I) revealed a single cluster of low-energy conformations for the

PC1-PC2 space, indicating that the complex was stable throughout the simulation process without any major changes in conformations. Electrostatic surface potential mapping of the compound, using an electrostatic surface potential map (as depicted in Fig. 3J), revealed that the Salviadione binding site is in a region with negative charges, which perfectly complements the positive charges in the compound.

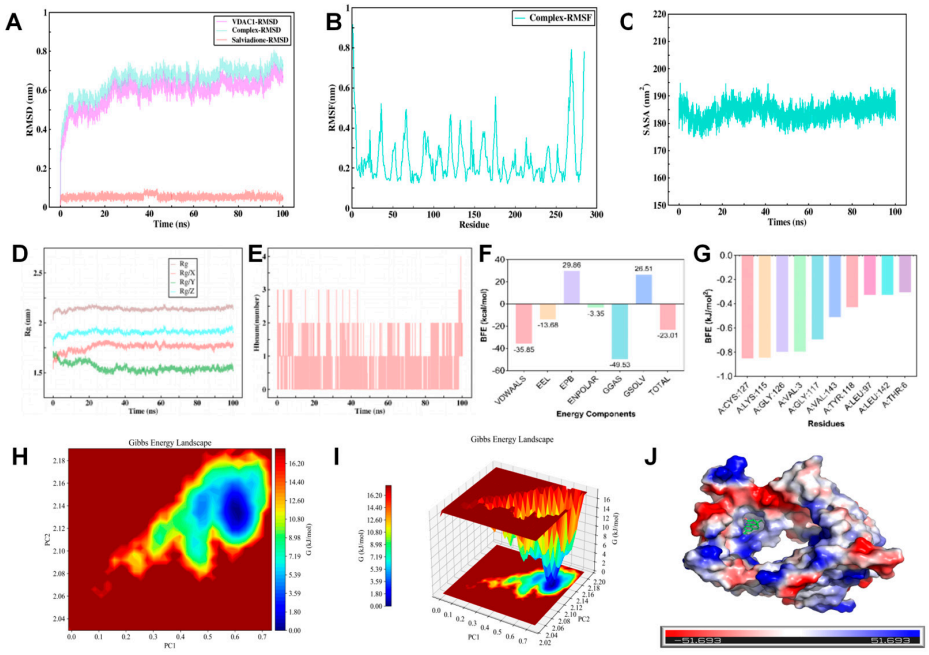

Figure 3: Molecular dynamics simulation analysis of the Salviadione-VDAC1 complex. (**A**) Root mean square deviation (RMSD) of the protein backbone, the ligand Salviadione, and the entire complex over the 100 ns simulation. (**B**) Root mean square fluctuation (RMSF) of VDAC1 protein residues. (**C**) Solvent accessible surface area (SASA) of the complex over the simulation time. (**D**) Radius of the total Rg of the complex. (**E**) Number of hydrogen bonds formed between Salviadione and VDAC1 throughout the simulation. (**F**) Molecular Mechanics/Generalized Born Surface Area (MM/GBSA) free energy decomposition per residue for the binding of Salviadione to VDAC1. (**G**) Bar plot of binding free energy contributions for key residues identified in (**F**). (**H**) Two-dimensional free energy landscape plotted as a function of RMSD and Rg. (**I**) Three-dimensional representation of the free energy landscape corresponding to (**H**). (**J**) Surface electrostatic potential map of the Salviadione-VDAC1 complex. Red regions represent negative potential, and blue regions represent positive potential. All simulations were performed using GROMACS with the AMBER14 force field. The MM/GBSA calculations were performed on the equilibrated trajectory (last 60 ns).

3.4 Salviadione Attenuates LPS-Induced Cytotoxicity in BEAS-2B Cells

To verify the protective effects of Salviadione against LPS-induced lung epithelial cell injury, the optimal concentrations of LPS and Salviadione were determined using cell viability tests. LPS treatment in a dose-dependent manner suppressed the viability of BEAS-2B cells (Fig. 4A), with 1 μg/mL LPS for 24 h suppressing cell viability to 40–60% of the control, which was used for the establishment of the inflammatory injury model. Similarly, we investigated the effects of various concentrations of Salviadione upon LPS-treated cells and found the restoration of cell viability in a dose-response manner (Fig. 4B). Significant protective potential was noted with 5, 10, and 20 μM, and no signs of cell toxicity were found. Therefore, in the next set of studies, these concentrations were used as low, medium, and high concentrations.

Treatment of cells with LPS at 1 μg/mL significantly reduced cell viability compared to controls. Co-treatment with Salviadione, however, restored viability in a concentration-dependent manner (Fig. 4C).

We found that the treatment with 10 μM Salviadione alone had no appreciable effect on the viability of cells, indicating that this is a non-cytotoxic concentration of Salviadione. Consistent with this, the LDH release assays revealed that LPS significantly enhanced LDH activity in the culture supernatant, and this was dose-dependently antagonized by Salviadione (Fig. 4D). Our observation that the highest level of conditioning of the culture medium by 10 μM Salviadione offered the best level of cell protective activity from all the concentrations tested by us is important. Here, Salviadione decreases LPS-induced damage to lung epithelial cells in a dose-dependent fashion without evoking any cell toxicity.

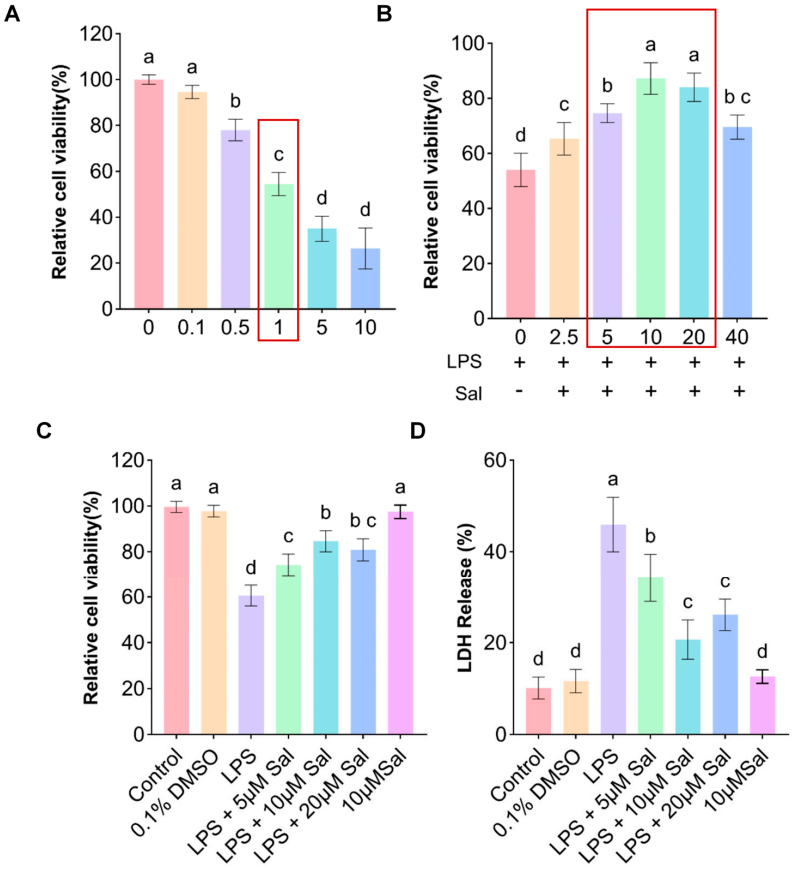

Figure 4: Salviadione protects against LPS-induced injury in BEAS-2B cells. (**A**) Cell viability after 24 h treatment with LPS at 0, 0.1, 0.5, 1, 5, or 10 μg/mL (n = 6). (**B**) Cell viability after 24 h co-treatment with LPS (1 μg/mL) and Salviadione (Sal) at 0, 2.5, 5, 10, 20, or 40 μM (n = 6). (**C**) Cell viability (CCK-8) after 24 h treatment: Control, Vehicle (0.1% DMSO), LPS (1 μg/mL), LPS with Sal (5, 10, or 20 μM), or Sal alone (10 μM) (n = 6). (**D**) Cytotoxicity (LDH release) under the same treatment conditions as (**C**) (n = 6). Data are mean ± SEM. Statistical analysis was performed using one-way ANOVA followed by Tukey's multiple-comparisons test. Lowercase letters (e.g., a, b, c, d) represent the results of overall pairwise comparisons across all groups. Groups sharing at least one common letter are not significantly different, whereas groups without shared letters are significantly different at $p < 0.05$. Because this annotation system reflects the overall adjusted comparison structure among all groups rather than only comparisons between adjacent concentrations, different assays may display different significance patterns depending on variance distribution and post hoc adjustment. Exact p-values for major pairwise comparisons are provided in Supplementary Table S1. The red box in panel (**A**) highlights the selected LPS concentration (1 μg/mL), which reduced cell viability to 40–60% of the control. The red box in panel (**B**) highlights the selected Salviadione concentrations (5, 10, and 20 μM) for subsequent experiments, as these doses significantly restored cell viability without causing cytotoxicity.

3.5 Salviadione Protects Mitochondrial Function by Inhibiting LPS-Induced Ferroptosis

We used specific ferroptosis-related as well as mitochondrial function marker molecule expression to evaluate whether ferroptosis plays a role in LPS-induced cell injury, as well as examining the influence of Salviadione on ferroptosis. LPS stimulation clearly showed an increase in intracellular lipid ROS (Fig. 5A) levels as well as in the amount of ferrous iron (Fe^{2+}) (Fig. 5B), in addition to downregulating the expression of the ferroptosis-related gene GPX4, whereas ACSL4 is upregulated (Fig. 5C). We used the inhibitor of ferroptosis, Ferrostatin-1 (Fer-1, 1 μM); it counteracted LPS-induced changes, including suppression of lipid peroxidation and iron overload, partial restoration of GPX4, and downregulation of ACSL4, proving ferroptosis. Of note, Salviadione (10 μM) showed comparable protective efficacy with Fer-1 in robustly suppressing the LPS-driven lipid ROS production and Fe^{2+} loading, while restoring GPX4 and ACSL4 expressions toward basal levels. By using the classical ferroptosis inducer Erastin (10 μM) as a positive control, we verified that Erastin indeed potently provoked the ferroptosis-related changes. Co-treatment with Salviadione weakened Erastin-induced lipid peroxidation, iron overload, and GPX4/ACSL4 dysregulation, further supporting its ferroptosis-inhibitory activity. Our experiments indicated that ferroptosis partially underlay LPS-induced injury of lung epithelial cells and Salviadione exerts a protective effect on such cells by way of inhibiting lipid peroxidation, stabilizing intracellular iron, and normalizing GPX4/ACSL4 expression.

In addition, the mitochondrial function status of VDAC1 and GPX4 was explored. Compared with the control, the cells treated with LPS (1 μg/mL) showed a significant decrease in ATP production in the cells (Fig. 5D), an increase in mitochondrial ROS levels (Fig. 5E), as well as a decrease in mitochondrial membrane potential status (Δψm) (Fig. 5F). Co-treatment with Salviadione (10 μM) successfully reversed these alterations by restoring ΔΨm, reducing mitochondrial ROS, and increasing ATP levels, while Salviadione alone did not affect the above parameters. By Western blotting, LPS treatment increased VDAC1 expression and decreased GPX4 expression, and COX IV, a mitochondrial inner membrane marker, showed no change (Fig. 5G). The Salviadione co-treatment significantly reduced LPS-induced changes of VDAC1 and returned GPX4 expression to basal levels without affecting COX IV expression. The above results indicate that Salviadione maintains mitochondrial membrane potential and relieves mitochondrial oxidative stress and improves energy metabolism injured by LPS, and it protects cells through regulating the expressions of VDAC1 and GPX4. As shown in Fig. 5H, LPS treatment significantly decreased GPX4 mRNA expression and increased ACSL4 mRNA expression compared with the control group ($p < 0.05$). Co-treatment with Salviadione (10 μM) significantly reversed these changes ($p < 0.05$ vs. LPS), bringing the mRNA levels back to near-control values. These transcriptional changes are consistent with the protein expression data shown in Fig. 5C.

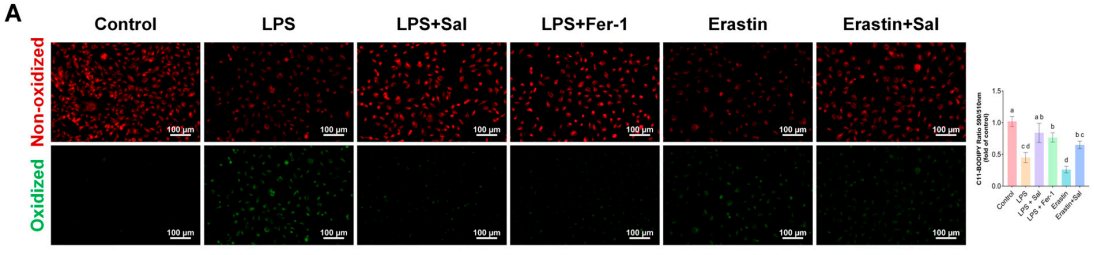

Figure 5: *Cont.*

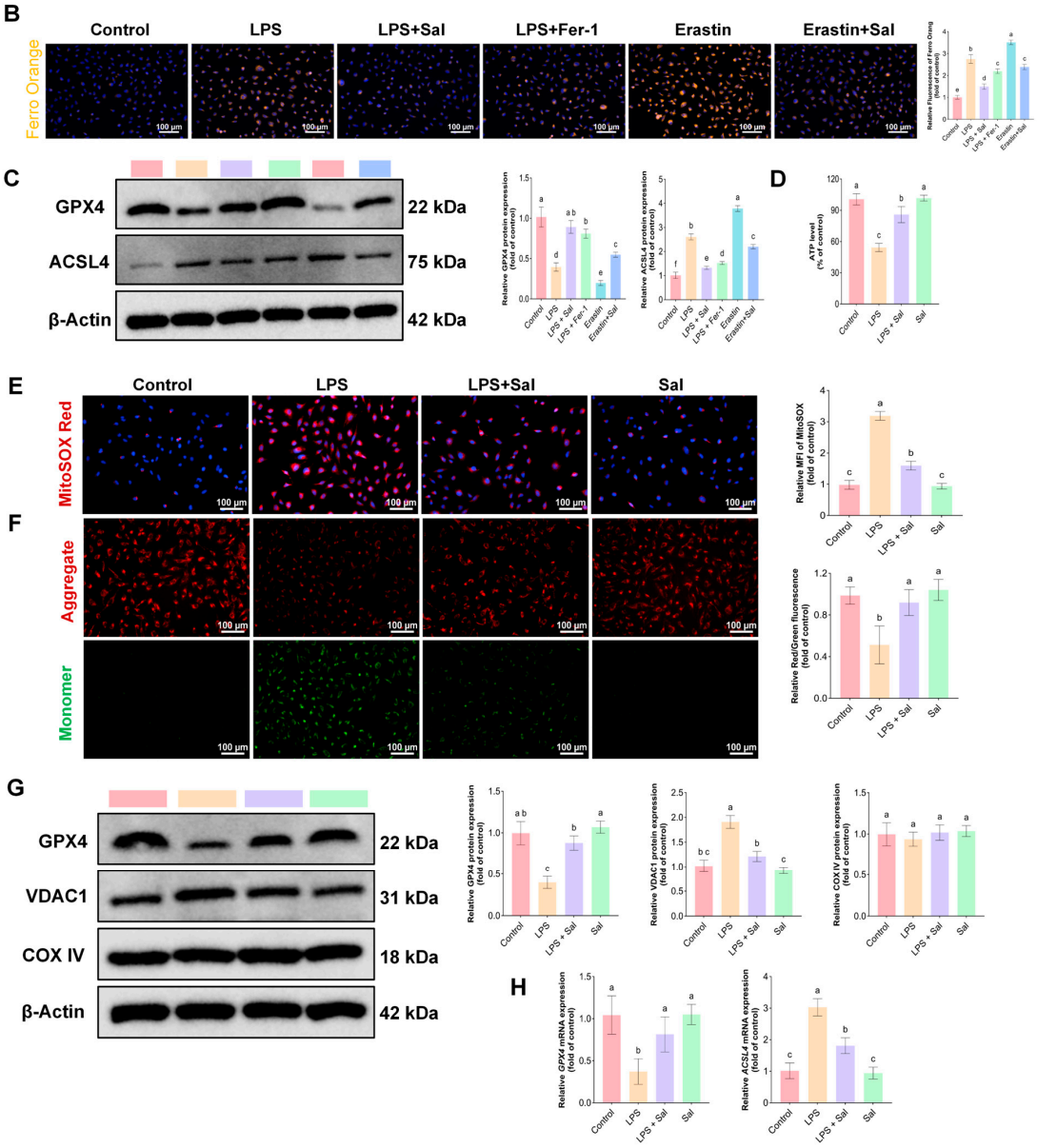

Figure 5: Salviadione inhibits LPS-induced ferroptosis and preserves mitochondrial function. (**A**) Lipid peroxidation with representative images after 24 h treatment: Control, LPS (1 μg/mL), LPS + Sal (10 μM), LPS + Fer-1 (1 μM), Erastin (10 μM), or Erastin + Sal (n = 3). (**B**) Intracellular Fe^{2+} level (FerroOrange fluorescence) under the same treatments as (A) (n = 3). (**C**) Protein levels of GPX4 and ACSL4 (Western blot) under the same treatments as (**A**) (n = 3). (**D**) Cellular ATP content with representative images after 24 h: Control, LPS, LPS + Sal, or Sal alone (n = 6). (**E**) Mitochondrial ROS (MitoSOX fluorescence) with representative images under the same treatments as (**D**) (n = 3). (**F**) Mitochondrial membrane potential (JC-1 red/green ratio) under the same treatments as (**D**) (n = 3). (**G**) Protein levels of VDAC1, GPX4, and COX IV (Western blot) under the same treatments as (**D**) (n = 3). (**H**) GPX4 and ACSL4 mRNA expression measured by qPCR under the same treatment conditions as (**C**). All quantitative data are mean ± SEM. Statistical analysis was performed using one-way ANOVA followed by Tukey's multiple-comparisons test. Lowercase letters (e.g., a, b, c, d) represent the results of overall pairwise comparisons across all groups. Groups sharing at least one common letter are not significantly different, whereas groups without shared letters are significantly different at $p < 0.05$.

3.6 Salviadione Exerts Protective Effects by Targeting VDAC1 to Suppress Ferroptosis

To understand the protective mechanism of Salviadione, knockdown experiments with siRNA were carried out to study the viability of VDAC1 in this protective mechanism. As shown in Fig. 6A, Western blot analysis was carried out to ensure knockdown of the VDAC1 protein with si-VDAC1, and qPCR analysis was conducted to ensure knockdown of VDAC1 mRNA (Fig. 6B). In the VDAC1 knockdown assay, it was shown that the compound Salviadione was not able to rescue the LPS-induced decrease in cell viability (Fig. 6C), nor was it able to suppress the LPS-induced lipid ROS accumulation (Fig. 6D). This demonstrates that the complete absence of VDAC1 prevents the protective effects of the compound Salviadione, thereby confirming its importance in the process.

To further verify whether Salviadione's protective effect is mediated by inhibition of ferroptosis, pharmacological intervention experiments were conducted. As shown in Fig. 6E,F, the ferroptosis inducer, RSL3, profoundly inhibited the restorative effect of Salviadione on cell viability, as well as its inhibition of lipid ROS accumulation, which is highly consistent with its inhibition of GPX4 expression (Fig. 6G). In contrast, co-treatment with ferroptosis inhibitor Ferrostatin-1 (Fer-1) synergistically enhanced Salviadione's protective effect, recovering the cell viability close to control levels, further maximally repressing lipid peroxidation, and maintaining elevated GPX4 expression. Altogether, findings from both VDAC1 knockdown and pharmacological modulation studies point toward the fact that Salviadione protects against LPS-induced lung epithelial cell injury by targeting VDAC1 and inhibiting the ferroptosis pathway.

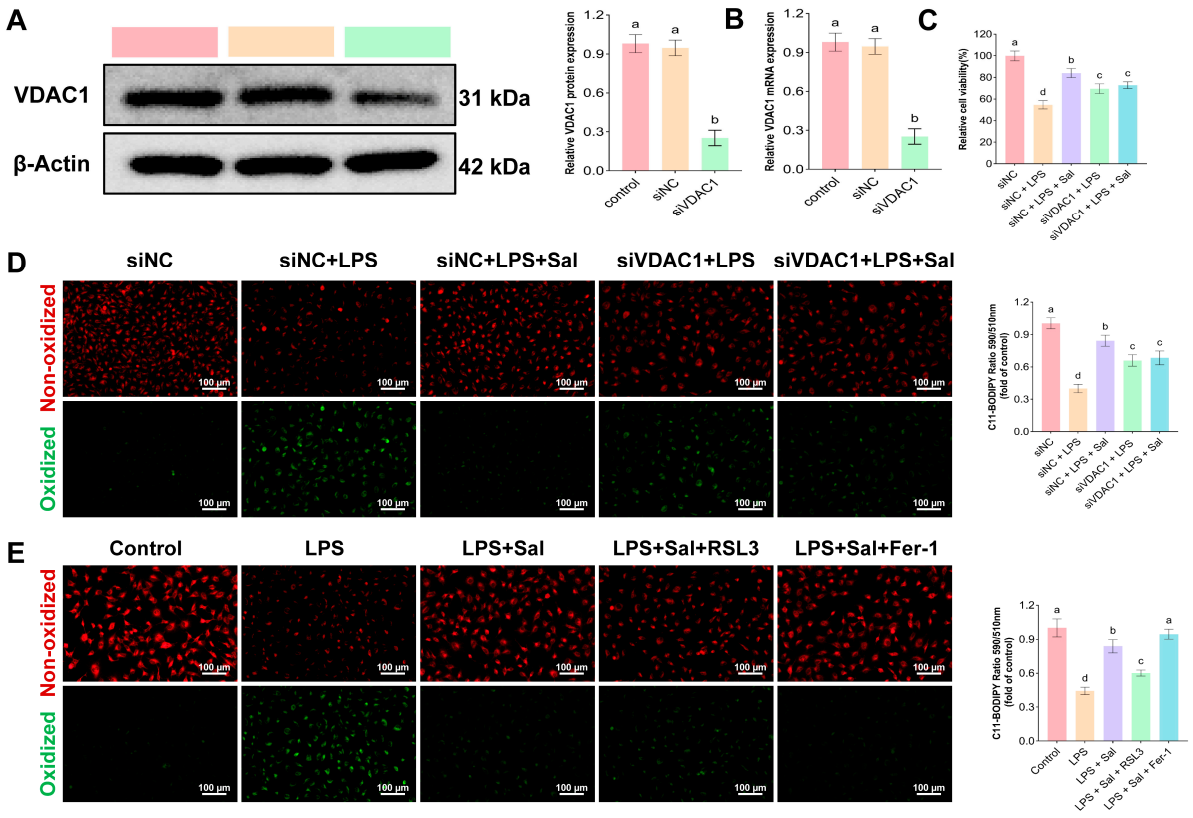

Figure 6: *Cont.*

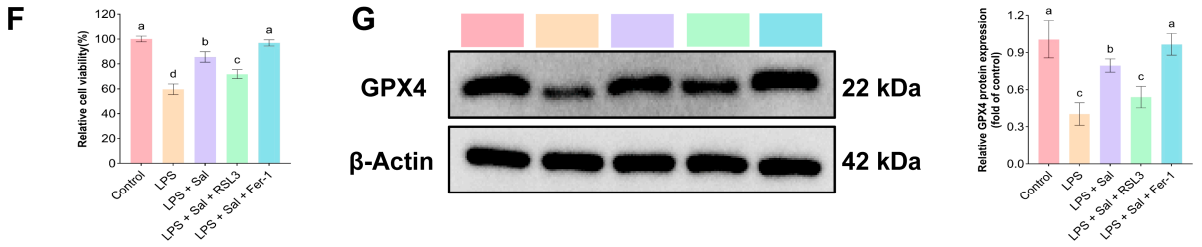

Figure 6: VDAC1 mediates the anti-ferroptotic effect of Salviadione. (**A**) VDAC1 protein expression analyzed by Western blot with densitometric quantification in cells transfected with si-NC or si-VDAC1 for 48 h (n = 3). (**B**) VDAC1 mRNA expression analyzed by qPCR under the same transfection conditions as (**A**) (n = 3). (**C**) Cell viability (CCK-8) in cells transfected as in (**A**) and then treated for 24 h with LPS (1 μg/mL) with or without Sal (10 μM) (n = 6). (**D**) Lipid peroxidation (C11-BODIPY 581/591 staining) shown with representative images and quantified as red/green fluorescence ratio under the same conditions as (**C**) (n = 3). (**E**) Lipid peroxidation (C11-BODIPY 581/591 staining) shown with representative images and quantified as red/green ratio under the same treatments as (**F**) (n = 3). (**F**) Cell viability (CCK-8) after 24 h treatment: LPS, LPS + Sal (10 μM), LPS + Sal + RSL3 (50 nM), or LPS + Sal + Fer-1 (1 μM) (n = 6). (**G**) GPX4 protein expression analyzed by Western blot with densitometric quantification under the same pharmacological treatments as (**E**) (n = 3). All quantitative data are mean ± SEM. Statistical analysis was performed using one-way ANOVA followed by Tukey's multiple-comparisons test. Lowercase letters (e.g., a, b, c, d) represent the results of overall pairwise comparisons across all groups. Groups sharing at least one common letter are not significantly different, whereas groups without shared letters are significantly different at $p < 0.05$.

4 Discussion

ALI-induced manifestations are marked by distinct inflammatory responses and an inability to regulate apoptosis [10,43–45]. Most recent literature indicates that ferroptosis, a type of cell death resulting from iron-mediated lipid peroxidation, may play a critical part in the pathogenesis of ALI [46]. However, specific and effective therapeutic agents for this process are lacking. Our study, based on network pharmacology prediction, molecular docking, and subsequent *in vitro* validation, demonstrates that Salviadione, an endogenous alkaloid, has the potential to protect lung epithelial cells against LPS-induced injury by affecting mitochondrial ferroptosis, particularly mediated by VDAC1, offering a novel therapeutic target for ALI intervention.

Network pharmacology and molecular docking techniques have been shown to be powerful methods to search for potential targets of medicines [47]. Through an integrative strategy combining various kinds of omics data and systematic pharmacological research, the study suggested that Salviadione might protect lung epithelial cells by regulating mitochondria-mediated ferroptosis, possibly through a VDAC1-GPX4 pathway. Network analysis indicated that whereas VDAC1 and GPX4 were found to be highly enriched among Salviadione-ALI overlapping targets, these genes were also found among the top 10 percent hub genes of the PPI network, thus indicating their importance in the regulation and function of these genes. GPX4, being an essential negative regulator of ferroptosis, preserves the integrity of cellular membranes by scavenging lipid hydroperoxide molecules in a manner independent of glutathione [48]. VDAC1, being the major pore-forming protein in the outer mitochondrial membrane, facilitates the movement of metabolites like glutathione and modulates mitochondrial ROS production [49]. Previous research has suggested the functional relationship between these two proteins with respect to ferroptosis [29,30]. In addition, our GSEA results revealed that the primary targets were actively involved in 'fatty acid metabolism', 'glutathione metabolism', and 'mitochondrial membrane transport', which play an essential role in ferroptosis, especially in the involvement of mitochondria in promoting lipid peroxidation. Thus, the

computational predictions provided here indicate the potential mechanism by which Salviadione operates to modulate the VDAC1-GPX4-mediated ferroptosis pathway in mitochondria. Such predictions indicate the exact direction that subsequent experimental evidence is expected to follow.

This proposed mechanism has been strenuously validated at the molecular and cellular levels. Molecular dynamics simulations verified that a stable binding conformation of Salviadione with VDAC1 indeed forms. Further, upon using siRNA to knock down VDAC1, it was found that the cytoprotective efficacy of Salviadione in promoting cell viability was largely abrogated, and the inhibitory efficacy in reducing lipid ROS formation was also significantly compromised, suggesting the importance of VDAC1 for Salviadione's function. Recent studies have supported the notion of VDAC1 as a "metabolic gatekeeper" in ferroptosis. This is achieved through the regulation of glutathione efflux and the opening of mPTP, thus impacting GPX4 activity and lipid peroxide levels, as our results showed. In addition, experiments of pharmacological intervention revealed that the ferroptosis inducer RSL3 dramatically abrogated the cytoprotective effect of Salviadione, while the ferroptosis inhibitor Ferrostatin-1 synergistically enhanced its efficacy, further confirming that its action depends on the ferroptosis pathway. Notably, we find that Salviadione, aside from counteracting the decrease in the GPX4 gene, also affected the regulation of the ACSL4 gene, potentially suggesting the ability to regulate lipid metabolic homeostasis via the "GPX4-ACSL4" balance, characteristic of known ferroptosis signaling pathways [50,51]. By integrating computational and experimental approaches, we reveal the validity of predictive target identification as well as the mechanistic significance underlying the protective ability of Salviadione.

Our discoveries revealed an integrated protective network in which the integrity of mitochondrial elements contributes to the inhibition of ferroptosis. In ALI, mitochondrial dysfunction appears to play a major and crucial role in initiating cell death associated with ferroptosis [52,53]. The above experimental data have clearly shown that Salviadione significantly attenuates the mitochondrial membrane potential disappearance of LPS, blocks the overproduction of mitochondrial ROS, and restores the intracellular ATP levels, specifically indicating that the cytoprotective action of Salviadione is initiated through maintaining cellular energy metabolism. Expanding upon this basis, Salviadione possesses marked antiferroptotic effects, dosage-dependently preventing lipid peroxidation and intracellular iron buildup, which are at the heart of the biochemistry leading to ferroptosis. Additional support for these agents is afforded in their interaction with VDAC1, which is the major mitochondrial outer membrane channel controlling mitochondrial metabolism and the production of ROS, thereby potentially controlling outcomes in the downstream sequence leading to ferroptosis [54,55].

From the above results, we can conclude that knockdown of VDAC1, besides inhibiting the positive regulation of mitochondrial function by Salviadione, also abrogates the potential that VDAC1 has for restoring GPX4 levels. This implies that VDAC1 might be the upstream regulator for GPX4, thereby modulating the activity of the latter. The proposed "VDAC1-mitochondrial function-GPX4" regulatory axis directly links the organelle dynamics of mitochondria to the ferroptotic cell death pathway. Direct evidence supporting a functional interaction between VDAC1 and GPX4 has recently emerged. Hu et al. demonstrated that resveratrol protects cardiomyocytes against ischemia/reperfusion-induced ferroptosis via the VDAC1/GPX4 pathway, and importantly, a direct interaction between VDAC1 and GPX4 was confirmed by co-immunoprecipitation [29]. More recently, Li et al. reported that Hsp90 C-terminal domain inhibition reduces GPX4 protein levels and disrupts the GPX4-VDAC1 interaction, leading to VDAC1 carbonylation and oligomerization, which in turn promotes ferroptosis [31,56,57]. These findings provide compelling evidence that VDAC1 indeed serves as an upstream regulator of GPX4 in the ferroptosis pathway.

Regarding whether Salviadione exerts its anti-ferroptotic effect through direct binding to GPX4, our molecular docking analysis revealed a favorable binding energy of −7.0 kcal/mol between Salviadione and GPX4 (Section 3.2), suggesting a potential direct interaction. Moreover, a recent study reported that a Salviadione derivative (compound 15a) inhibits inflammation by directly binding to and inhibiting RIPK2 [58], indicating that Salviadione and its derivatives are capable of direct target engagement. Although the precise binding between Salviadione and GPX4 remains to be validated by biophysical methods (e.g., surface plasmon resonance or isothermal titration calorimetry), our computational and functional data strongly suggest that direct GPX4 binding may contribute to the anti-ferroptotic mechanism of Salviadione. Several limitations of this study should be acknowledged. First, all experiments were performed *in vitro* using a single cell line (BEAS-2B); therefore, *in vivo* validation using animal models is necessary to confirm the translational potential of Salviadione. Second, although our data support a functional link between VDAC1 and GPX4, the precise molecular mechanism by which VDAC1 regulates GPX4 expression or activity remains to be fully defined. Third, while this study focused on ferroptosis, Salviadione may also modulate other inflammatory pathways in ALI (e.g., NF-κB or NLRP3 inflammasome), which warrants further investigation. Addressing these limitations in future studies will help establish Salviadione as a candidate therapeutic agent for ALI.

We acknowledge that all *in vitro* experiments in this study were performed using a single human bronchial epithelial cell line (BEAS-2B). While this cell line is a well-established and widely accepted model for studying ALI/ARDS, it does not fully recapitulate the complex cellular microenvironment of the lung or the potential contributions of primary alveolar epithelial cells. Therefore, the generalizability of our findings may be limited. Future studies using primary human alveolar epithelial cells or *in vivo* animal models (e.g., LPS-induced acute lung injury in mice) are necessary to validate the therapeutic potential of Salviadione and to further explore the VDAC1/GPX4 axis in a more physiological context. Such studies would also allow assessment of Salviadione's pharmacokinetic properties and its effects on multiple cell types (e.g., macrophages, endothelial cells) in the inflamed lung. Additionally, the upstream signaling pathways that regulate VDAC1 expression or activity in the context of ALI remain to be explored and represent an important direction for future research.

From a translational perspective, VDAC1 is an attractive therapeutic target because it is accessible to small molecules, and Salviadione represents a promising lead compound for developing VDAC1-targeted interventions in ALI.

5 Conclusion

In this study, by using prediction based on network pharmacology, molecular docking, and *in vitro* validation, the molecular mechanisms by which Salviadione exerts cytoprotective effects in LPS-challenged human lung epithelial cells are unraveled. Salviadione targets important proteins, VDAC1, and GPX4, maintains mitochondrial membrane potential, decreases mitochondrial ROS production, and increases cellular ATP levels to maintain cellular energy metabolism. Concurrently, it upregulates GPX4 expression while suppressing lipid peroxidation and intracellular iron accumulation, thereby providing coordinated protection at both the levels of mitochondrial function preservation and ferroptosis inhibition. Our findings demonstrate that Salviadione represents a potential natural therapeutic for acute lung injury. They also support the VDAC1–GPX4 regulatory axis as a target, providing a robust rationale for designing treatments that modulate the mitochondria–ferroptosis pathway.

Acknowledgement: Not applicable.

Funding Statement: The authors received no specific funding for this study.

Author Contributions: The authors confirm contribution to the paper as follows: study conception and design: Ke Ma, Wentao Su; data collection: Aishan Gulijiakela, Jihao Xiong, San Zhang; analysis and interpretation of results: Wentao Su, Aishan Gulijiakela, Ke Ma; draft manuscript preparation: Wentao Su, Aishan Gulijiakela. All authors reviewed and approved the final version of the manuscript.

Availability of Data and Materials: The original transcriptomic dataset analyzed during the current study is available in the Gene Expression Omnibus (GEO) repository https://www.ncbi.nlm.nih.gov/geo/query/acc.cgi?acc=GSE226486.

Ethics Approval: Not applicable.

Conflicts of Interest: The authors declare no conflicts of interest.

Supplementary Materials: The supplementary material is available online at https://www.techscience.com/doi/10.32604/biocell.2026.081235/s1.

References

1. Wan C, Liu X, Xu Y, Kang L, Yu X, Wang M, et al. Polydatin in respiratory diseases: Multi-target mechanisms and therapeutic potential. Front Pharmacol. 2026;17:1752467. [CrossRef].
2. Huang KY. Influence of liriodendrin on NLRP3-mediated pyroptosis and proinflammatory pathways in mice experiencing acute respiratory distress syndrome induced by lipopolysaccharide. Biocell. 2025;49(2):315–34. [CrossRef].
3. Long ME, Mallampalli RK, Horowitz JC. Pathogenesis of pneumonia and acute lung injury. Clin Sci. 2022;136(10):747–69. [CrossRef].
4. Butt Y, Kurdowska A, Allen TC. Acute lung injury: A clinical and molecular review. Arch Pathol Lab Med. 2016;140(4):345–50. [CrossRef].
5. Xu H, Sheng S, Luo W, Xu X, Zhang Z. Acute respiratory distress syndrome heterogeneity and the septic ARDS subgroup. Front Immunol. 2023;14:1277161. [CrossRef].
6. Liu SW, Chen YJ, Liu Y, Zhou W, Liu X. Regulated programmed cell death in acute lung injury: From pathogenesis to therapy. Front Immunol. 2025;16:1630015. [CrossRef].
7. Xia S, Gu X, Wang G, Zhong Y, Ma F, Liu Q, et al. Regulated cell death of alveolar macrophages in acute lung inflammation: Current knowledge and perspectives. J Inflamm Res. 2024;17:11419–36. [CrossRef].
8. Mokrá D. Acute lung injury—From pathophysiology to treatment. Physiol Res. 2020;69(Suppl 3):S353–66. [CrossRef].
9. Wang J, Chao J. Alveolar epithelial cell dysfunction in acute respiratory distress syndrome: Mechanistic insights and targeted interventions. Biomedicines. 2025;13(9):2299. [CrossRef].
10. Liu H, Dong J, Xu C, Ni Y, Ye Z, Sun Z, et al. Acute lung injury: Pathogenesis and treatment. J Transl Med. 2025;23(1):926. [CrossRef].
11. Mowery NT, Hillman Terzian WT, Nelson AC. Acute lung injury. Curr Probl Surg. 2020;57(5):100777. [CrossRef].
12. Jin X, Tang J, Qiu X, Nie X, Ou S, Wu G, et al. Ferroptosis: Emerging mechanisms, biological function, and therapeutic potential in cancer and inflammation. Cell Death Discov. 2024;10(1):45. [CrossRef].
13. Lv L, Wang Y, Lv X, Miao Q. Involvement of HMGB1-mediated ferroptosis in systemic diseases. Front Cell Dev Biol. 2025;13:1676941. [CrossRef].
14. Chen J, Gou Z, Yang G, Zhou L, Kim AN, Shi W, et al. Ferroptosis, a distinct form of cell death, and research progress on its modulators. Pharmaceuticals. 2025;18(12):1785. [CrossRef].
15. Li J, Deng SH, Li J, Li L, Zhang F, Zou Y, et al. Obacunone alleviates ferroptosis during lipopolysaccharide-induced acute lung injury by upregulating Nrf2-dependent antioxidant responses. Cell Mol Biol Lett. 2022;27(1):29. [CrossRef].
16. Lai K, Song C, Gao M, Deng Y, Lu Z, Li N, et al. Uridine alleviates sepsis-induced acute lung injury by inhibiting ferroptosis of macrophage. Int J Mol Sci. 2023;24(6):5093. [CrossRef].

17. Shi J, Song S, Wang Y, Wu K, Liang G, Wang A, et al. Esketamine alleviates ferroptosis-mediated acute lung injury by modulating the HIF-1α/HO-1 pathway. Int Immunopharmacol. 2024;142(Pt A):113065. [CrossRef].
18. Sun B, Wang L, Zhang T. Role of ferroptosis in alveolar epithelial cells in acute respiratory distress syndrome. J Inflamm Res. 2025;18:9679–98. [CrossRef].
19. Yao M, Liao J, Liu Z, Zhao W, Song S, Huang X, et al. Ferroptosis: A key driver and therapeutic target in the pathogenesis of acute respiratory distress syndrome. Front Immunol. 2025;16:1567980. [CrossRef].
20. Chen Z, Tang H, Gan S, Yang C, Li S, Li J, et al. Ferroptosis mediates airway epithelial E-cadherin dysfunction in LPS-induced acute lung injury. Pulm Pharmacol Ther. 2024;84:102284. [CrossRef].
21. Li Y, Cao Y, Xiao J, Shang J, Tan Q, Ping F, et al. Inhibitor of apoptosis-stimulating protein of p53 inhibits ferroptosis and alleviates intestinal ischemia/reperfusion-induced acute lung injury. Cell Death Differ. 2020;27(9):2635–50. [CrossRef].
22. Zhang W, Liu Y, Liao Y, Zhu C, Zou Z. GPX4, ferroptosis, and diseases. Biomed Pharmacother. 2024;174:116512. [CrossRef].
23. Li J, Jia YC, Ding YX, Bai J, Cao F, Li F. The crosstalk between ferroptosis and mitochondrial dynamic regulatory networks. Int J Biol Sci. 2023;19(9):2756–71. [CrossRef].
24. Shoshan-Barmatz V, Israelson A, Brdiczka D, Sheu SS. The voltage-dependent anion channel (VDAC): Function in intracellular signalling, cell life and cell death. Curr Pharm Des. 2006;12(18):2249–70. [CrossRef].
25. Keinan N, Tyomkin D, Shoshan-Barmatz V. Oligomerization of the mitochondrial protein voltage-dependent anion channel is coupled to the induction of apoptosis. Mol Cell Biol. 2010;30(24):5698–709. [CrossRef].
26. Zhou X, Tang X, Li T, Li D, Gong Z, Zhang X, et al. Inhibition of VDAC1 rescues $A\beta_{1\text{-}42}$-induced mitochondrial dysfunction and ferroptosis via activation of AMPK and Wnt/β-catenin pathways. Mediators Inflamm. 2023;2023:6739691. [CrossRef].
27. Yang J, Lu X, Hao JL, Li L, Ruan YT, An XN, et al. VSTM2L protects prostate cancer cells against ferroptosis via inhibiting VDAC1 oligomerization and maintaining mitochondria homeostasis. Nat Commun. 2025;16(1):1160. [CrossRef].
28. Ingold I, Berndt C, Schmitt S, Doll S, Poschmann G, Buday K, et al. Selenium utilization by GPX4 is required to prevent hydroperoxide-induced ferroptosis. Cell. 2018;172(3):409–22.e21. [CrossRef].
29. Hu T, Zou HX, Zhang ZY, Wang YC, Hu FJ, Huang WX, et al. Resveratrol protects cardiomyocytes against ischemia/reperfusion-induced ferroptosis via inhibition of the VDAC1/GPX4 pathway. Eur J Pharmacol. 2024;971:176524. [CrossRef].
30. Feng Y, Madungwe NB, Imam Aliagan AD, Tombo N, Bopassa JC. Liproxstatin-1 protects the mouse myocardium against ischemia/reperfusion injury by decreasing VDAC1 levels and restoring GPX4 levels. Biochem Biophys Res Commun. 2019;520(3):606–11. [CrossRef].
31. Li J, Wu G, Su H, Liang M, Cen S, Liao Y, et al. Hsp90 C-terminal domain inhibition enhances ferroptosis by disrupting GPX4-VDAC1 interaction to increase HMOX1 release from oligomerized VDAC1 channels. Redox Biol. 2025;85:103672. [CrossRef].
32. Stockwell BR, Friedmann Angeli JP, Bayir H, Bush AI, Conrad M, Dixon SJ, et al. Ferroptosis: A regulated cell death nexus linking metabolism, redox biology, and disease. Cell. 2017;171(2):273–85. [CrossRef].
33. Jiang X, Stockwell BR, Conrad M. Ferroptosis: Mechanisms, biology and role in disease. Nat Rev Mol Cell Biol. 2021;22(4):266–82. [CrossRef].
34. Shen Y, Zhang G, Wei C, Zhao P, Wang Y, Li M, et al. Potential role and therapeutic implications of glutathione peroxidase 4 in the treatment of Alzheimer's disease. Neural Regen Res. 2025;20(3):613–31. [CrossRef].
35. Kibble M, Saarinen N, Tang J, Wennerberg K, Mäkelä S, Aittokallio T. Network pharmacology applications to map the unexplored target space and therapeutic potential of natural products. Nat Prod Rep. 2015;32(8):1249–66. [CrossRef].
36. Merecz-Sadowska A, Sadowski A, Zielińska-Bliźniewska H, Zajdel K, Zajdel R. Network pharmacology as a tool to investigate the antioxidant and anti-inflammatory potential of plant secondary metabolites—a review and perspectives. Int J Mol Sci. 2025;26(14):6678. [CrossRef].
37. Cemali SH, Poyraz S, Belveren S, Taş S, Ali Tamer M, Döndaş NY, et al. Recent insights in multi-target drugs in pharmacology and medicinal chemistry. ChemMedChem. 2025;20(18):e202500447. [CrossRef].

38. Li L, Ding C, Zou C, Xiong Z, Zhu W, Qian J, et al. A novel salviadione derivative, compound 15a, attenuates diabetes-induced renal injury by inhibiting NF-κB-mediated inflammatory responses. Toxicol Appl Pharmacol. 2020;409:115322. [CrossRef].
39. Jaber N, Emond C, Cazier F, Billet S. Toxicological response of the BEAS-2B cell after acute exposure at the air-liquid interface to ethylbenzene and m-xylene alone and in binary mixtures. J Appl Toxicol. 2025;45(9):1770–86. [CrossRef].
40. Landskroner EA, Tsai CS. Impact of ethanol as a vehicle for water-insoluble pollutants in BEAS-2B cell toxicity assays. Toxicol Mech Methods. 2025;35(9):1437–49. [CrossRef].
41. Liu Y, Zhou J, Luo Y, Li J, Shang L, Zhou F, et al. Honokiol alleviates LPS-induced acute lung injury by inhibiting NLRP3 inflammasome-mediated pyroptosis via Nrf2 activation *in vitro* and *in vivo*. Chin Med. 2021;16(1):127. [CrossRef].
42. Baoyinna B, Miao J, Oliver PJ, Ye Q, Shaheen N, Kalin T, et al. Non-lethal doses of RSL3 impair microvascular endothelial barrier through degradation of sphingosie-1-phosphate receptor 1 and cytoskeletal arrangement in a ferroptosis-independent manner. Biomedicines. 2023;11(9):2451. [CrossRef].
43. Johnson ER, Matthay MA. Acute lung injury: Epidemiology, pathogenesis, and treatment. J Aerosol Med Pulm Drug Deliv. 2010;23(4):243–52. [CrossRef].
44. Zhang L, Li H, Li D, Dai Q. Unraveling the synergy of inflammation and apoptosis in sepsis-induced acute lung injury: Insights and therapeutic perspectives (review). Mol Med Rep. 2026;33(1):1–18. [CrossRef].
45. Fan E, Brodie D, Slutsky AS. Acute respiratory distress syndrome: Advances in diagnosis and treatment. JAMA. 2018;319(7):698–710. [CrossRef].
46. Bai Y, Ma Y, Li X. The research progress of ferroptosis in acute lung injury. Biochem Biophys Rep. 2026;45:102434. [CrossRef].
47. Hopkins AL. Network pharmacology: The next paradigm in drug discovery. Nat Chem Biol. 2008;4(11):682–90. [CrossRef].
48. Guo S, Liu J, Hua J, Ding L, Chen Q. Ferroptosis: The pivotal link in cardiovascular diseases pathogenesis and therapy. Int J Gen Med. 2025;18:7675–97. [CrossRef].
49. Hu F, Hu T, He A, Yuan Y, Wang X, Zou C, et al. Puerarin protects myocardium from ischaemia/reperfusion injury by inhibiting ferroptosis through downregulation of VDAC1. J Cell Mol Med. 2024;28(24):e70313. [CrossRef].
50. Chen C, Lu J, Qu Y, Dong J, Hong Y, Ren Y, et al. MNQ derivative D19 alleviates LPS-induced inflammation and oxidative stress in sheep follicular granulosa cells through the GPX4-mediated ferroptosis. Front Vet Sci. 2025;12:1621738. [CrossRef].
51. Fan BY, Pang YL, Li WX, Zhao CX, Zhang Y, Wang X, et al. Liproxstatin-1 is an effective inhibitor of oligodendrocyte ferroptosis induced by inhibition of glutathione peroxidase 4. Neural Regen Res. 2021;16(3):561–6. [CrossRef].
52. Zhou K, Qin Q, Lu J. Pathophysiological mechanisms of ARDS: A narrative review from molecular to organ-level perspectives. Respir Res. 2025;26(1):54. [CrossRef].
53. Tumurkhuu G, Koide N, Dagvadorj J, Morikawa A, Hassan F, Islam S, et al. The mechanism of development of acute lung injury in lethal endotoxic shock using α-galactosylceramide sensitization. Clin Exp Immunol. 2008;152(1):182–91. [CrossRef].
54. Jang SK, Ahn SH, Kim G, Kim S, Hong J, Park KS, et al. Inhibition of VDAC1 oligomerization blocks cysteine deprivation-induced ferroptosis via mitochondrial ROS suppression. Cell Death Dis. 2024;15(11):811. [CrossRef].
55. Shoshan-Barmatz V, De S, Meir A. The mitochondrial voltage-dependent anion channel 1, Ca^{2+} transport, apoptosis, and their regulation. Front Oncol. 2017;7:60. [CrossRef].
56. Liu Y, Zhou L, Xu Y, Li K, Zhao Y, Qiao H, et al. Heat shock proteins and ferroptosis. Front Cell Dev Biol. 2022;10:864635. [CrossRef].
57. Chen X, Kang R, Kroemer G, Tang D. Organelle-specific regulation of ferroptosis. Cell Death Differ. 2021;28(10):2843–56. [CrossRef].
58. Hu CH, Chen Y, Jin TY, Wang Z, Jin B, Liao J, et al. A derivative of tanshinone IIA and salviadione, 15a, inhibits inflammation and alleviates DSS-induced colitis in mice by direct binding and inhibition of RIPK2. Acta Pharmacol Sin. 2025;46(3):672–86. [CrossRef].